

The effect of dark matter resolution on the collapse of baryons in high redshift numerical simulations

John A. Regan^{1*}, Peter H. Johansson¹ & John H. Wise²

¹*Department of Physics, University of Helsinki, Gustaf Hållströmin katu 2a, FI-00014 Helsinki, Finland*

²*Center for Relativistic Astrophysics, Georgia Institute of Technology, 837 State Street, Atlanta, GA 30332, USA*

10 November 2021

ABSTRACT

We examine the impact of dark matter particle resolution on the formation of a baryonic core in high resolution adaptive mesh refinement simulations. We test the effect that both particle smoothing and particle splitting have on the hydrodynamic properties of a collapsing halo at high redshift ($z > 20$). Furthermore, we vary the background field intensity, with energy below the Lyman limit (< 13.6 eV), as may be relevant for the case of metal-free star formation and super-massive black hole seed formation. We find that using particle splitting methods greatly increases our particle resolution without introducing any numerical noise and allows us to achieve converged results over a wide range of external background fields. Additionally, we find that for lower values of the background field a lower dark matter particle mass is required. We define the radius of the core as the point at which the enclosed baryonic mass dominates over the enclosed dark matter mass. For our simulations this results in $R_{\text{core}} \sim 5$ pc. We find that in order to produce converged results which are not affected by dark matter particles requires that the relationship $M_{\text{core}}/M_{\text{DM}} > 100.0$ be satisfied, where M_{core} is the enclosed baryon mass within the core and M_{DM} is the minimum dark matter particle mass. This ratio should provide a very useful starting point for conducting convergence tests before any production run simulations. We find that dark matter particle smoothing is a useful adjunct to already highly resolved simulations.

Key words: Cosmology: theory – large-scale structure – first stars, methods: numerical

1 INTRODUCTION

Gravitational collapse of dark matter has been well studied over the past four decades with increasingly high resolution N-body numerical simulations (Davis et al. 1985; Frenk et al. 1988; Warren et al. 1992; Cen et al. 1994; Gelb & Bertschinger 1994; Navarro et al. 1996, 1997; Hernquist et al. 1996; Jenkins et al. 2001; Wambsganss et al. 2004; Springel et al. 2008; Diemand et al. 2008; Bosch et al. 2014) leading to the confirmation that the large-scale structure of the Universe is built up through hierarchical collapse of small dark matter haloes. It is within the gravitational potential wells of these dark matter structures that galaxies and their associated active galactic nuclei and quasars form (White & Rees 1978; White & Frenk 1991; Springel et al. 2005; Croton et al. 2006; Johansson et al. 2012; Vogelsberger et al. 2014).

Dark matter is modelled as a collisionless fluid and in principle can be solved using the collisionless Boltzmann equation (e.g. Shlosman et al. 1979; Rasio et al. 1989; Hozumi 1997). However, the computational demands of solving this six dimensional equation means that instead dark matter is typically treated in a Monte-Carlo fashion (however see recent work by Hahn & Angulo 2015) and represented by a set of collisionless particles which interact with each other gravitationally. Solving the gravitational interactions of a many-body system is then dealt with in one of two ways, direct summation (e.g. von Hoerner 1960; Aarseth 1963; von Hoerner 1963; Steinmetz 1996) or more commonly, in cosmological simulations, using an approximate treatment involving a Tree algorithm (Barnes & Hut 1986, 1989) or a particle mesh algorithm (Efsthathiou et al. 1985; Hockney & Eastwood 1988) - see also Bertschinger (1998) for a comprehensive review.

The subsequent addition of gas dynamics to the simulations increases the complexity of the simulations sub-

* E-mail: john.regan@helsinki.fi

stantially, requiring not just a detailed treatment of the gas (fluid) interaction with the dark matter, but also of a range of physical processes involving the gas including radiative cooling, star formation and the tracking of individual chemical species. Incorporating the gas dynamics into the simulation usually also takes the form of one of two mechanisms - smoothed particle hydrodynamics (SPH) (Lucy 1977; Gingold & Monaghan 1977) or grid based methods (Ryu et al. 1990; Cen et al. 1990; Stone & Norman 1992; Bryan et al. 1995) where the hydrodynamical equations are solved on the grid using finite difference techniques possibly involving deforming or adaptive meshes (e.g. Springel 2010; Bryan et al. 2014).

Here we focus on the effect the mass resolution of the dark matter particles can have on the gas dynamics within a collapsing halo where the gas densities can exceed the dark matter densities by several orders of magnitude as happens in the centres of newly forming galaxies, mini-haloes and clusters of galaxies. In order to conduct this case study we use the **Enzo** code (see §2 for details on **Enzo**) to follow the collapse of gas within collapsing haloes early in the Universe at a time when the cooling of the gas is driven by primordial processes and in which the gas has not yet been enriched with metals from previous episodes of star formation. This case is relevant for simulations involving the first generation of stars (Pop III stars) (Abel et al. 2002; Bromm et al. 2002; Yoshida et al. 2003; Bromm & Larson 2004; Yoshida et al. 2006; O’Shea & Norman 2008; Yoshida et al. 2008; Wise & Abel 2008; O’Shea & Norman 2008; Turk et al. 2009; Bromm et al. 2009; Clark et al. 2011a; Stacy et al. 2010, 2012; Susa et al. 2014; Stacy & Bromm 2014; Hirano et al. 2014) or for the case of direct collapse models of supermassive black holes (Shlosman et al. 1989; Haiman & Loeb 2001; Oh & Haiman 2002; Bromm & Loeb 2003; Haiman 2006; Begelman et al. 2006; Wise et al. 2008; Regan & Haehnelt 2009a,b; Regan et al. 2014a,b) which are also thought to form out of pristine gas at high redshift.

Previous studies of dark matter resolution have indicated the negative numerical effects that dark matter can have on the collapse of baryons in the context of galaxy formation. Steinmetz & White (1997) showed that using dark matter particles with masses above a critical mass limit (their work was focused in the context of galaxy formation) introduced spurious two body heating effects which they found completely suppressed the effects of radiative cooling. Although their numerical tests were carried out using the SPH technique they argued that the results are valid in the case of grid based approaches also given the modelling of the dark matter component is similar in both instances. And while other studies have noted the effect that dark matter mass resolution plays in galaxy formation simulations (e.g. Machacek et al. 2001; Kaufmann et al. 2006) no specific study has been made, to the best of our knowledge, on the effect of dark matter resolution on the collapsing core¹ within an embryonic

galaxy. This is particularly crucial as correctly accounting for the cooling and heating effect becomes extremely important in determining the characteristics of the final object. In this paper we study this exact effect.

It is also worth noting that apart from the negative impact that poorly resolved dark matter particles may have on the baryonic physics an additional numerical artefact may occur if a dark matter particle flies into the high density region from a lower density region. This “flyby” and the perturbing effects of its large mass may then induce incorrect physical conditions. While we do not specifically deal with this issue in this study it can be alleviated using particle smoothing (see §2.4) which will necessarily prevent adverse effects from a large dark matter mass within the baryon dominated core.

We vary the mass resolution of the dark matter particles that surround the collapsing core in an effort to identify any spurious heating effects that the dark matter has on the collapsing core and identify resolution guidelines. Furthermore, we vary the background radiation field resulting in the formation (and collapse) of mini-haloes and haloes with virial temperatures $T > 10^4$ K and again test for dark matter mass resolution convergence.

The paper is laid out as follows: in §2 we describe the numerical approach used and the various techniques employed that can affect the dark matter resolution; in §3 we describe the characteristics of the simulations used in this study; in §4 we describe the results of our numerical simulations; in §5 we discuss the parameters for choosing the correct dark matter particle mass and in §6 we present our conclusions. Throughout this paper we assume a standard Λ CDM cosmology with the following parameters (Planck Collaboration et al. 2014, based on the latest Planck data), $\Omega_{\Lambda,0} = 0.6817$, $\Omega_{m,0} = 0.3183$, $\Omega_{b,0} = 0.0463$, $\sigma_8 = 0.8347$ and $h = 0.6704$. We further assume a spectral index for the primordial density fluctuations of $n = 0.9616$.

2 NUMERICAL SETUP

We have used the publicly available adaptive mesh refinement (AMR) code **Enzo**². AMR codes are a popular tool for studying the gravitational and hydrodynamical collapse of astrophysical objects (although see for example Yoshida et al. 2006, Clark et al. 2011b & Mayer et al. 2014 among others for collapse simulations conducted using SPH techniques) due to their inherent ability to extend over many magnitudes in dynamic range. Therefore using **Enzo** as the code with which to perform this study is an obvious choice. Furthermore, we use version 3.0³ which is the bleeding edge version of the code incorporating a range of new features (e.g. Goldbaum et al. in prep).

Enzo was originally developed by Greg Bryan and Mike Norman at the University of Illinois (Bryan & Norman 1995, 1997; Norman & Bryan 1999; O’Shea et al. 2004; Bryan et al. 2014). The gravity solver in **Enzo** uses an N -Body adaptive particle-mesh technique (Efsthathiou et al.

¹ The core radius is here defined as the radius at which the baryonic enclosed mass exceeds the dark matter mass for the first time. Typically, for our simulations this occurs between 1 and 10 parsecs from the point of highest density. This definition is closely related to the Jeans length, λ_J , of the gas for a gas with an isothermal temperature of 8000 K and number density, $n \sim 1 \times 10^6 \text{ cm}^{-3}$.

² <http://enzo-project.org/>

³ Changeset: 6037:1c232317e50d

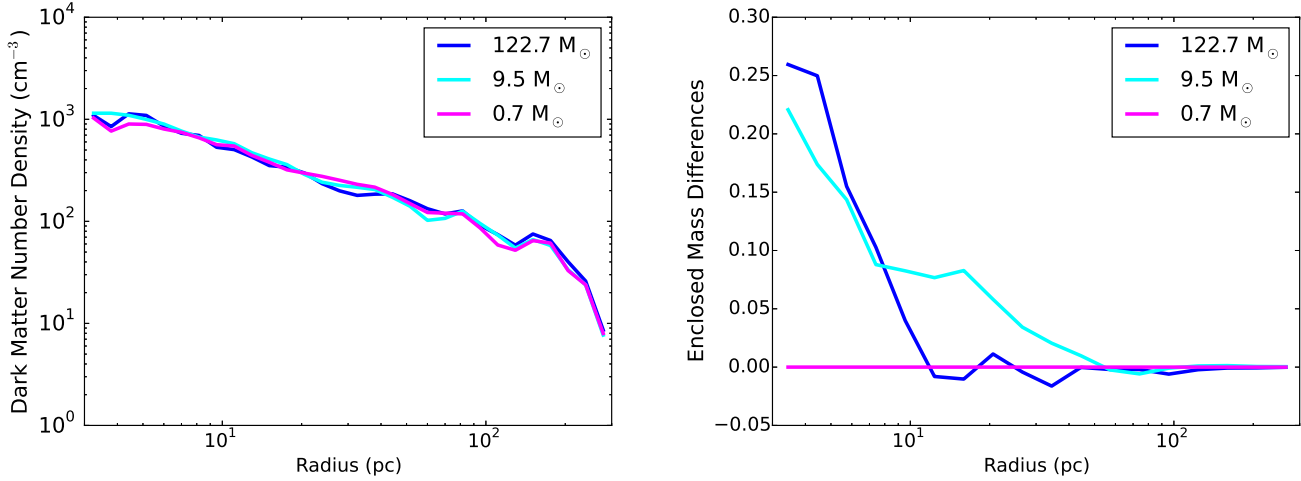


Figure 1. The left hand panel shows the spherically averaged dark matter density profile for a dark matter only simulation of Halo A. The output is taken at a redshift of $z = 23$ and the density is scaled by the mass of the hydrogen atom to enable a direct comparison with the gas density. The lines are for a minimum dark matter mass of $122.7 M_{\odot}$, $9.5 M_{\odot}$ and $0.7 M_{\odot}$. The right hand panel shows the difference between the enclosed mass profile for the same halo at the same output time. The differences are calculated against the highest resolution simulation (i.e. the dark matter simulation with $M = 0.7 M_{\odot}$).

1985; Hockney & Eastwood 1988; Couchman 1991) while the hydrodynamics are evolved using the piecewise parabolic method combined with a non-linear Riemann solver for shock capturing. The AMR methodology allows for additional finer meshes to be laid down as the simulation runs to enhance the resolution in a given, user defined, region.

For our simulations we set the maximum refinement level to 18. Refinement is triggered in *Enzo* when the refinement criteria are exceeded. The refinement criteria used in this work were based on three physical measurements: (1) The dark matter particle over-density, (2) The baryon over-density and (3) the Jeans length. The first two criteria introduce additional meshes when the over-density ($\frac{\Delta\rho}{\rho_{\text{mean}}}$) of a grid cell with respect to the mean density exceeds 8.0 for baryons and/or DM. Furthermore, we set the *MinimumMassForRefinementExponent* parameter to -0.1 making the simulation super-Lagrangian and therefore reducing the threshold for refinement as higher densities are reached. For the final criteria we set the number of cells per Jeans length to be 16 in these runs.

2.1 Chemical Modelling

We adopt a nine species model for the chemical network used including H , H^+ , He , He^+ , He^{++} , e^- , H_2 , H_2^+ and H^- . The gas is allowed to cool radiatively during the collapse. Additionally, we incorporate an external radiation field with an energy below the hydrogen ionisation edge into the simulations conducted here. Specifically we incorporate radiation energies from 0.76 eV up to 13.6 eV which affects the three species H^- , H_2 , H_2^+ as described in more detail below. The intensity of the background radiation is varied over a range of values between 0 and $500 \times 10^{-21} \text{ erg cm}^{-2} \text{ s}^{-1} \text{ Hz}^{-1} \text{ sr}^{-1}$ with the effective temperature of the blackbody temperature set to $T = 50000 \text{ K}$ in all cases. We use the variable J_{21} as shorthand for $10^{-21} \text{ erg cm}^{-2} \text{ s}^{-1} \text{ Hz}^{-1} \text{ sr}^{-1}$. We initially

concentrate our study on radiation fields with 80 J_{21} and 500 J_{21} and then in §4.3 we explore the effect of varying the external field. The shape of the spectrum is fully described by the temperature of the blackbody radiation, T_{eff} and the amplitude of the fluctuation, κJ_{21} , where κ is any scalar quantity. We normalise the external radiation field at the hydrogen ionisation edge. In our simulations we allow the external field to affect the rates of three species - H^- , H_2 , H_2^+ , the rates for the three species are given below (Abel et al. 1997):

$$k_{\text{H}^-} = \frac{4\pi}{h} \int_{0.76}^{13.6} J_{21} \frac{B(E, T_{\text{eff}})}{B(13.6, T_{\text{eff}})} \frac{\sigma(E)}{E} dE \quad [\text{s}^{-1}]$$

$$k_{\text{H}_2} = 1.38 \times 10^9 J_{21} \frac{B(E_{\text{LW}}, T_{\text{eff}})}{B(13.6, T_{\text{eff}})} \quad [\text{s}^{-1}] \quad (1)$$

$$k_{\text{H}_2^+} = \frac{4\pi}{h} \int_{2.65}^{13.6} J_{21} \frac{B(E, T_{\text{eff}})}{B(13.6, T_{\text{eff}})} \frac{\sigma(E)}{E} dE \quad [\text{s}^{-1}]$$

where k_X is the photoionisation rate for a given species, J_{21} is the external field with implied units of $10^{-21} \text{ erg cm}^{-2} \text{ s}^{-1} \text{ Hz}^{-1} \text{ sr}^{-1}$, $\sigma(E)$ is the cross section at a given energy (frequency) and $B(E, T_{\text{eff}})$ is the blackbody spectrum at an energy, E , temperature, T_{eff} and E_{LW} is the energy in the Lyman-Werner band (12.8 eV). The integration limits are in eV and do not exceed the hydrogen ionisation threshold of 13.6 eV.

2.2 Realisations

Using the initial conditions generator *MUSIC* (Hahn & Abel 2011) we generated over 5000 random dark matter realisations with *Enzo* using a 256^3 grid. Each simulation was run until a redshift of $z = 30$ with an inline “Friends of Friends” halo finder. Several realisations were identified as

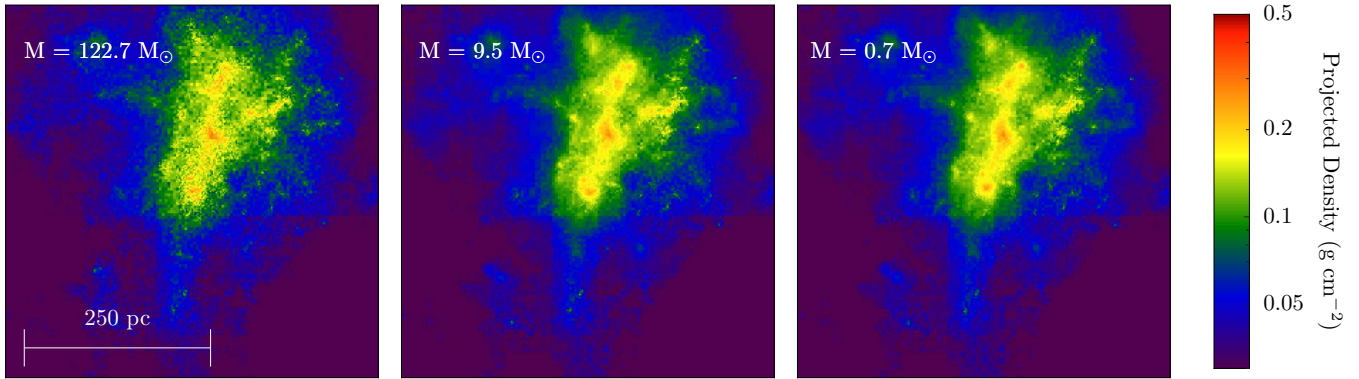


Figure 2. Each panel shows a dark matter density projection of the 0.5 kpc (physical) surrounding the collapsing halo at a redshift of $z = 23$. The left hand panel has a minimum dark matter mass of $M_{\text{DM}} \sim 122.7 M_{\odot}$, the middle panel has a minimum dark matter mass of $M_{\text{DM}} \sim 9.5 M_{\odot}$, and the right hand panel has a minimum dark matter mass of $M_{\text{DM}} \sim 0.7 M_{\odot}$. Each projection is centred on the point of maximum density in the simulation with a dark matter particle mass of $M_{\text{DM}} \sim 122.7 M_{\odot}$.

having a high sigma peak ($\sigma > 4.0$ at $z > 30$, see for example Regan et al. 2014a for details on the definition of σ). Three realisations were found from the initial dark matter runs and a single halo realisation was used to conduct this study - labeled *Halo A*. It should be noted that we have also conducted resolution tests on the two other haloes found - *Halo B* and *Halo C* - however the results were broadly similar. We discuss the characteristics of *Halo B* and *Halo C* in §4.4 but focus the bulk of this study around *Halo A*.

Each realisation was then resimulated with baryons included and with different levels of nested grids and hence dark matter particle resolution. We ran simulations utilising one, two and three levels of grid nesting. Each nested grid reduces the dark matter particle mass resolution by a factor of eight. Memory limitations restrict the number of nested grids to a maximum of three. For this study we use a box size of $2.0 h^{-1}$ Mpc which allows us to find large haloes (high sigma peaks) while also restricting the dynamic range required by the simulation. This means that the maximum dark matter particle resolution that *Enzo* can achieve in the simulation is $M_{\text{DM}} \sim 103 M_{\odot}$. *Enzo* does not dynamically refine the particle mass during the simulation when refining its grids. In order to refine the dark matter particles further we employ a Particle Splitting procedure.

2.3 Particle Splitting

In order to increase the resolution of the dark matter particles still further we employ the particle splitting techniques of Kitsionas & Whitworth (2002), several other authors have previously adopted the same technique (Yoshida et al. 2006; Greif et al. 2011; Kim et al. 2011; Hirano et al. 2014). We split particles at a redshift of $z = 40$ so as to minimise the effects of any noise introduced by the splitting technique. In particle splitting, the distribution of matter within a region assumes that the region has a uniform mass distribution and so no new perturbation modes are added. Splitting the particles at a redshift of 40 ensures that we approximate this case and furthermore we test for convergence as described below.

Particles are either split once or twice. Each splitting reduces the particle mass by a factor of 13 producing 13 new child particles in the process and so also increasing the computational demands of the simulation. We follow Kitsionas & Whitworth (2002) in choosing to split each parent particle into 13 child particles, the choice of 13 is somewhat arbitrary but attempts to take into account two competing arguments - 1) there should not be too large a difference between the child mass and the parent mass and 2) the collective density distribution of the family of children should approximate the spherically symmetric density distribution of the parent.

We test for convergence using both one and two iterations of splitting. We split the particles in a subregion surrounding the point of maximum density. The location of the point of maximum density is found from previous simulations where particle splitting was not used. This allows for the increased mass resolution to be targeted in the region surrounding the collapse. We select a region of $43.75 h^{-1}$ kpc (comoving) within which to do the first iteration of particle splitting. The second splitting, if performed, is done within a region half this size - $21.88 h^{-1}$ kpc (comoving). This allows for maximum dark matter resolution alongside maximum grid resolution.

In order to investigate any systematic effect on the dark matter particle properties we initially conducted dark matter only simulations where we split the particles at a redshift of $z = 40$ and subsequently looked at the highest density region approximately 80 Myrs later at a redshift of $z = 23$. In the runs with baryons the collapse occurs at a redshift of approximately $z = 23$ or earlier and so examining the forming dark matter halo at a redshift of $z = 23$ is appropriate.

In Figure 1 we show the dark matter density profiles and enclosed mass profiles for *Halo A* at a redshift of $z = 23$. The profiles are all centred at the point of maximum density as found in the simulation where particle splitting was not conducted (i.e. the simulation with a dark matter particle mass of $M_{\text{DM}} = 122.7 M_{\odot}$). In the left hand panel the density profile shows clearly that the differences between the run with no particle splitting (blue line) and the runs with par-

Table 1. Halo Details

Halo Name ^a	M _{Tot} ^b	M _{DM} ^c	M _{Baryon} ^d	R ₂₀₀ ^e	T _{vir} ^f	n _{H,max} ^g
Halo A	2.3×10^7	2.0×10^7	3.0×10^6	0.35	9718	1.05×10^9
Halo B	2.3×10^7	2.0×10^7	3.0×10^6	0.34	9098	1.01×10^9
Halo C	1.4×10^7	1.2×10^7	1.6×10^6	0.30	7402	1.18×10^9

Notes: The above table contains the simulation name^a, the total mass^b (gas & dark matter) at the virial radius⁴ [M_\odot], the enclosed mass in dark matter^c at the virial radius [M_\odot], the enclosed mass in baryons^d at the virial radius [M_\odot], the virial radius^e [kpc], the virial temperature^f [K], and the maximum gas number density^g in the halo [cm^{-3}]. All units are physical, unless explicitly stated otherwise.

ticle splitting (cyan and magenta lines) are negligible which gives us confidence that the dark matter splitting introduces little or no additional perturbing effects to the dark matter component. This should not be surprising since the splitting occurs early in the halo formation process at a time when the non-linear effects of the gravitational collapse are still negligible. To further emphasise the point we show the difference between the enclosed mass profiles for the same outputs. We normalise against the the highest resolution simulation (i.e. the simulation with a dark matter particle mass of $M_{\text{DM}} = 0.7 M_\odot$). The differences are negligible at large radii ($R \gtrsim 100$ pc) and increase to only a factor of $\lesssim 0.3$ at small scales.

Figure 2 shows a density projection of the dark matter density along the x-axis for this halo (Halo A) for each case. The left hand panel has a minimum dark matter particle mass of $M_{\text{DM}} = 122.7 M_\odot$, the middle panel has a minimum dark matter mass of $M_{\text{DM}} = 9.5 M_\odot$ and the right hand panel has a minimum dark matter mass of $M_{\text{DM}} = 0.7 M_\odot$. The halo becomes smoother as the dark matter resolution is increased but otherwise remains visually the same. The spatial scale in each case is given in the left panel and corresponds to 250 pc physical.

2.4 Particle Smoothing

In regions of high density (resolution) the cell size can become very small and the particles can begin to experience spurious two body effects. In order to avoid such spurious interactions the dark matter particles can be “smoothed” onto the grid once the cell size drops below a given threshold. In *Enzo* this is controlled via the *MaximumParticleRefinementLevel* parameter. Once the cell size drops below a user defined threshold the dark matter mass is interpolated onto the grid with some smoothing length h (which will always be quoted in comoving units). While computationally inefficient to do, it is done in only a very small region and so its effect on the overall computational time is small. The dark matter now effectively behaves as a continuous, rather than discrete, distribution in these very high density regions and the effects of (large) dark matter particles coming into close contact is alleviated. In this study we set the threshold value of h to 2.8 *comoving* parsecs (equivalent to a refinement level of 12). We run simulations where the smoothing is initiated and also where the smoothing is not activated. In the runs without the smoothing the smoothing length is effectively the minimum cell size (i.e. the cell size at maximum refinement level) which in the case of our simulations is 0.04 *comoving* parsecs at level 18.

2.5 External Radiation Fields

As noted above we concentrate our study on external radiation fields with values of 80 J_{21} and 500 J_{21} both of which may be relevant for studying the direct collapse of super-massive black holes at high redshift (Shlosman et al. 1989; Begelman et al. 2006; Dijkstra et al. 2008; Regan & Haehnelt 2009b,a; Shang et al. 2010; Johnson et al. 2013; Latif et al. 2013, 2014a,b; Agarwal et al. 2014; Regan et al. 2014a,b). A value of 80 J_{21} sets the field to where H_2 formation is inhibited but not completely destroyed, the collapse of the halo therefore takes place in an environment where the collapse is not isothermal. A value of 500 J_{21} on the other hand results in an isothermal collapse. By examining both scenarios the effects of different dark matter resolutions on the direct collapse model can be fully assessed.

We further assess the impact of smaller radiation fields on the collapse. We use field strengths of both 1 J_{21} and 10 J_{21} and we also test the case where no background exists (i.e. 0 J_{21}). All of these fields may be relevant for the case where metal-free stars form (e.g. Bromm et al. 1999; Abel et al. 2002; Bromm et al. 2002). A comparison of the affect of different field strengths is discussed in §4.3.

We do not examine the affect of changing the H_2 three body formation rates in this work and instead use the rates of Martin et al. (1996) throughout. This topic has been examined comprehensively by both Turk et al. (2011a) and Bovino et al. (2014). The Martin et al. (1996) rates are found to provide the most consistent fit from the work of Turk et al. (2011a), are density dependent and follow closely the rates of Forrey (2013) which are advocated by Bovino et al. (2014).

3 SIMULATION DETAILS

The primary goal of this study is to evaluate the impact, if any, of the dark matter resolution on the results of the collapse of the gas. The general halo characteristics of Halo A, Halo B and Halo C are given in Table 1. The study focuses on Halo A for the most part with the characteristics of Halo B and Halo C only discussed in §4.4.

Each (re)simulation of Halo A differs in either the minimum dark matter particle size or the minimum smoothing

⁴ The virial mass is defined as 200 times the mean density of the Universe in this case.

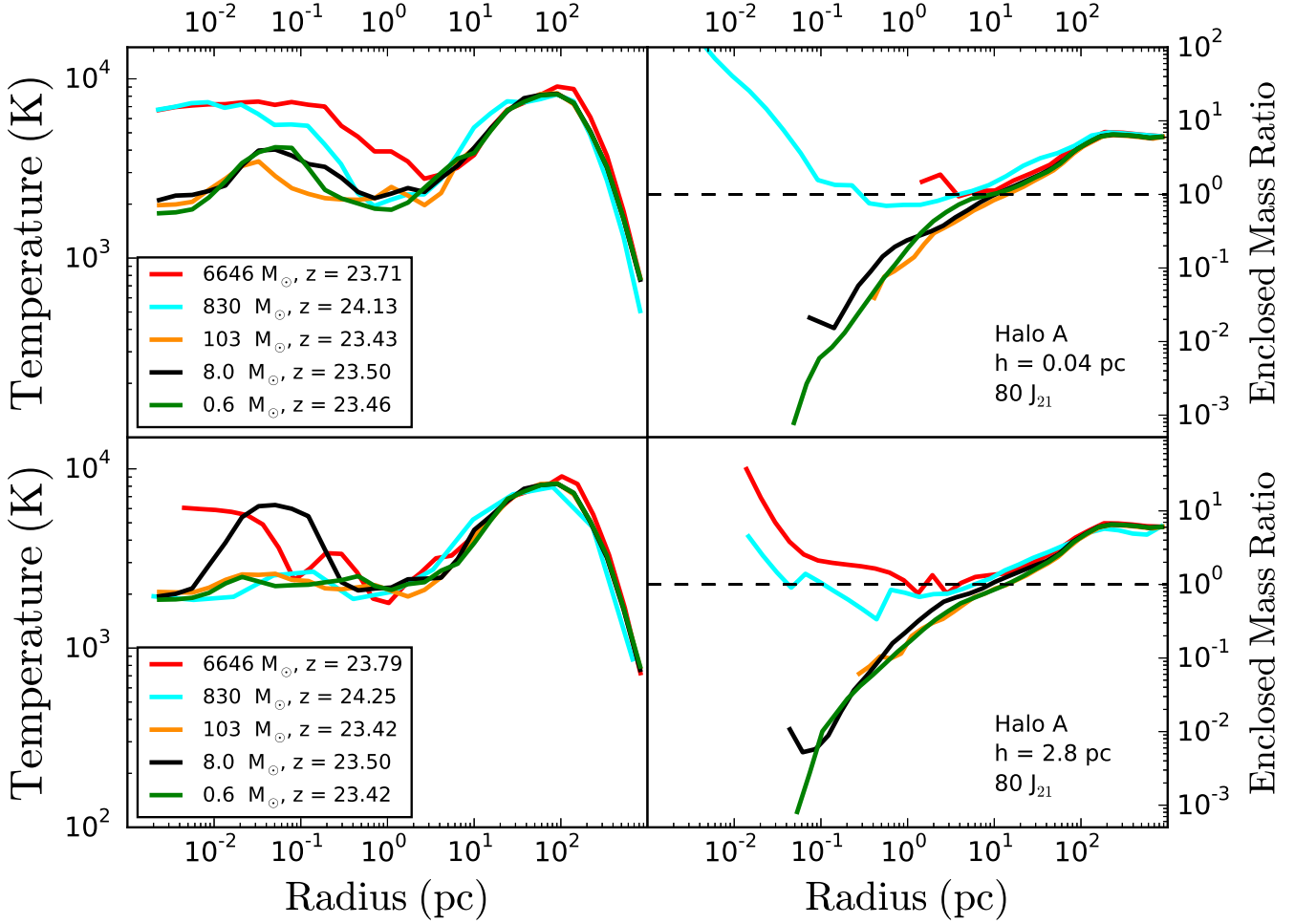


Figure 3. *Halo A*: In the top two panels no smoothing of the dark matter particles is activated and so the smoothing length is the same as the minimum cell size - 0.04 pc (comoving). In the bottom two panels the smoothing is activated at a refinement level of 12 (2.8 pc comoving). The bottom right panel shows the enclosed dark matter mass divided by the enclosed baryon mass - $M_{\text{DM}}/M_{\text{Baryon}}$. See text for further details on the plot characteristics.

length of the dark matter particle. Furthermore, the external radiation field that a simulation is exposed to is varied between 0 J_{21} and 500 J_{21} . The simulations are automatically halted once the maximum refinement level is reached. Therefore each simulated halo, which is exposed to the same external radiation field, also has a very similar maximum density and comparisons are made at this maximum refinement level output. Each simulation is therefore compared at a very similar stage in its evolution.

The smoothing lengths for each run are set either at the maximum refinement level which corresponds to 0.04 (refinement level 18) comoving pc or they are smoothed at a refinement level of 12 which corresponds to 2.80 comoving pc (see §2.4 for more details on setting the particle smoothing lengths). Each parameter used in each simulation is clearly marked in the left hand plot window of each figure. To promote clarity we refer to a simulation with a dark matter particle resolution of $0.6 M_{\odot}$ as S06, a simulation with a dark matter particle resolution of $8.0 M_{\odot}$ as S8, etc.

4 RESULTS

4.1 Halo A - Varying the Mass Resolution and Smoothing Lengths

We begin by examining the temperature profile for the collapsed haloes for the different dark matter mass resolutions and smoothing lengths. In the following cases the field strength is set to either 80 J_{21} or 500 J_{21} , we will examine the case of lower background radiation intensities in §4.3.

In Figure 3 we show the results for Halo A when the external field is fixed at 80 J_{21} . The top row in the panel shows simulations where no smoothing of the dark matter particles occurs. The bottom panel shows simulations where the smoothing is activated at a refinement level of 12 (2.8 comoving parsecs). Each simulation was run with different minimum dark matter particle resolution ranging from $M_{\text{DM}} = 6646 M_{\odot}$ to $M_{\text{DM}} = 0.6 M_{\odot}$. Looking at the left hand column where we have plotted the temperature profiles, centred on the densest point in the simulation, we see that down to approximately 1 parsec from the centre the

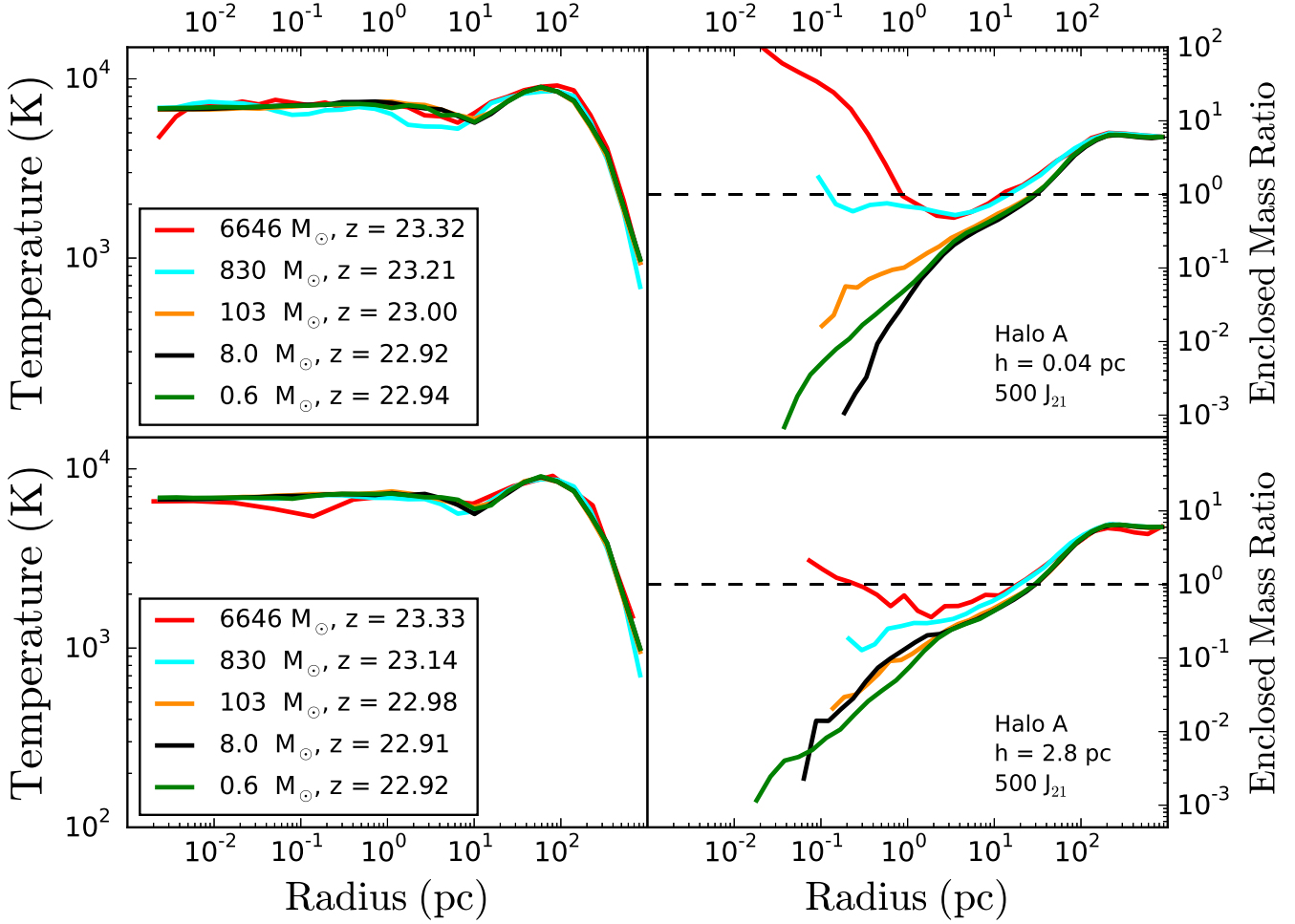


Figure 4. *Halo A*: Same as Figure 3 except the external radiation field is set to $500 J_{21}$.

smoothed and non-smoothed simulations agree very well. Within the core of the halo differences begin to appear. In the non-smoothed simulations (top left panel) the two lowest resolution simulations show a hotter core compared to the higher resolution simulations (i.e. those with a particle resolution $M_{\text{DM}} \leq 103 M_{\odot}$). In the smoothed runs the lowest resolution simulation has a temperature in the core of $T_{\text{core}} \sim 6000$ K while all the other simulations converge to a core temperature $T_{\text{core}} \sim 2000$ K - note also that S8 shows some significant heating within the core at a radius of approximately 0.05 pc. It should also be noted here that we do not include the effects of radiation self-shielding in our simulations which may be important in the core of the halo.

The right hand column yields a partial explanation for this. Considering first the non-smoothed runs in the top right panel - in both S830 and S6646 the core is dark matter dominated. The right hand panel plots the ratio of the enclosed dark matter mass to the enclosed gas mass. Values greater than 1.0 indicate regions where the dark matter dominates compared to the gas. In simulations S830 and S6646 the region inside approximately 1 parsec is dark matter dominated (in S6646 a single dark matter particle sits

approximately 1 parsec from the maximum gas density but its mass dominates the region). The results from S830 and S6646 are therefore likely to be spurious as the dark matter resolution in each case is insufficient and the dark matter mass ends up dominating the central potential. The heating of the core, seen in the left hand panel, should therefore be treated with caution due to the presence of perturbing forces from these large dark matter particles.

For the case of the smoothed simulations we again plot the dark matter to gas enclosed mass ratios in the bottom right panel. In this case we again see that S6646 is dark matter dominated and that S830 is only marginally gas dominated. The higher resolution simulations (S103, S8 and S06) on the other hand are all strongly gas dominated. Again in this case S6646 and S830 should be treated with caution (even though S830 shows converged results).

Regarding the temperature dichotomy within the core seen in the left hand column, the result is not as bad as it first appears and reflects the time at which we choose to examine the core. Excluding S830 and S6646 we see that S06, S8 and S103 all agree quite well (with the possible exception of the smoothed S8 simulation which shows a bump at ap-

proximately 0.05 pc). However, allowing the simulations to run at the maximum refinement level for a short time longer results in the core heating up in *each case*. This results from the collisional dissociation of H_2 which pushes the core onto the atomic cooling track once again - this is shown in the left panel of Figure 9 and discussed in more detail in Appendix A (as it lies somewhat outside the scope of the current work). We further caution the reader that running at the maximum refinement level means we are artificially preventing collapse which may induce unphysical results and that further research needs to be done to examine this scenario in more detail.

Strong convergence between S06, S8 and S103 is therefore achieved, when the external field is set to 80 J_{21} , but the study indicates that the lower resolution simulations dissociate the H_2 faster compared to the higher resolution simulations, driven by spurious dark matter effects, which impact the hydrodynamics.

In Figure 4 we show the results when the background radiation is set to 500 J_{21} with all other parameters remaining unchanged. In this case the external radiation field is strong enough to reduce the H_2 fraction by several orders of magnitude within the halo. The left hand column of Figure 4 shows the temperature profiles which show highly converged results for both the non-smoothed (top panel) and smoothed (bottom panel) for even the lowest dark matter resolutions. The right hand column shows the dark matter to gas enclosed mass ratio. The S6646 simulations are dark matter dominated in both cases (and yet the temperature profiles remain converged) but the S830 simulation is more gas dominated in the smoothed simulations compared to the non-smoothed case. The higher resolution runs also show stronger convergence when smoothed.

4.2 Halo A - Comparing Smoothed and non-Smoothed Simulations

The effect of smoothing the particles onto the grid is most noticeable in the low resolution simulations (i.e. S6646 & S803) while the effects become less pronounced once the dark matter particle mass drops or equivalently once the discretisation velocity, V_{disc} , becomes less than the local sound speed (equal to a few km/s at these temperatures). We define V_{disc} roughly as the velocity that a dark matter particle can impart onto its surroundings

$$V_{\text{disc}} = \sqrt{\frac{GM_{\text{DM}}}{R_s}} \quad (2)$$

where G is the usual gravitational constant, M_{DM} is the mass of a single dark matter particle and R_s is the smoothing length. This relationship can also be recast in terms of a discretisation temperature resulting in the equation

$$T_{\text{disc}} = \sqrt{\frac{\mu m_H GM_{\text{DM}}}{R_s k_b}} \quad (3)$$

where μ is the mean molecular weight, set to be 1.22 in this study, and k_b is the Boltzmann constant. This equation can be further expanded by replacing R_s with $\max(R, R_s)$ where R is any radius becoming

$$T_{\text{disc}}(R) = \sqrt{\frac{\mu m_H GM_{\text{DM}}}{\max(R, R_s) k_b}} \quad (4)$$

Equation 4 can then be used to determine the radius at which, for a given dark matter particle mass, the dark matter (under-)resolution can begin to influence the baryon temperature. We will return to this point in §4.3.

If we compare the non-smoothed simulations to the smoothed ones when the radiation field is set to 80 J_{21} (i.e. upper and lower rows of Figure 3) we see that the temperature profiles in the left hand panels both show a significant scatter. The mass ratios are qualitatively similar (right hand panels) in both the smoothed and non-smoothed runs with the higher resolution (S103, S8 and S06) well converged but with S6646 and S830 showing significant scatter between the smoothed and non-smoothed runs. For example, the S830 run in the smoothed simulation is marginally gas dominated while in the non-smoothed case S830 is strongly dark matter dominated. The overall effect of smoothing when the radiation field is set to 80 J_{21} is therefore marginal, the higher resolution simulations are already well converged and so smoothing only improves the convergence slightly. The lower resolution runs are dark matter dominated and smoothing cannot prevent this although smoothing may somewhat lessen the adverse effects.

In comparing the cases where the external radiation field is stronger with J set to 500 J_{21} the effects are only slightly more encouraging. In the 500 J_{21} case the gas is warmer and hence the sound speed is correspondingly higher meaning that the discreteness effects, quantified by V_{disc} are somewhat lessened. This has the effect that for the temperature profiles the results appear completely converged as the effects of the radiation overwhelm any spurious dark matter effects. Nonetheless in both the 80 J_{21} case and the 500 J_{21} case the S6646 simulation is strongly dark matter dominated and smoothing the dark matter onto the grid at this stage only alleviates slightly this particular ill effect. However, in the case of S830 we observe that while in the non-smoothed case the core is marginally gas dominated it is significantly gas dominated in the smoothed case - although the ratio remains above 0.1. Finally similar to the 80 J_{21} case the simulations with a particle mass $M_{\text{DM}} \lesssim 103 M_\odot$ are relatively well converged in both the smoothed and non-smoothed cases although the smoothed case does show less deviation at the smallest scales.

Therefore, the result is that smoothing tends to improve convergence only in isolated cases or when the dark matter resolution is already high. However, smoothing poorly resolved dark matter particles onto the grid will likely have no positive effect and it is therefore more important to adequately resolve a given region with a sufficiently high dark matter mass resolution *and* then to smooth the particles onto the grid to remove any lingering discrete effects from the dark matter particles.

4.3 Halo A - Changing the External Field Amplitude

So far we have selected only external fields of 80 J_{21} or 500 J_{21} . These fields are relevant for investigating the case of a collapsing halo exposed to a nearby strong UV source as may be required in the direct collapse formation model (e.g. Dijkstra et al. 2008; Visbal et al. 2014). We now turn our attention to investigating the effects of other external field amplitudes which may be expected at this redshift. In par-

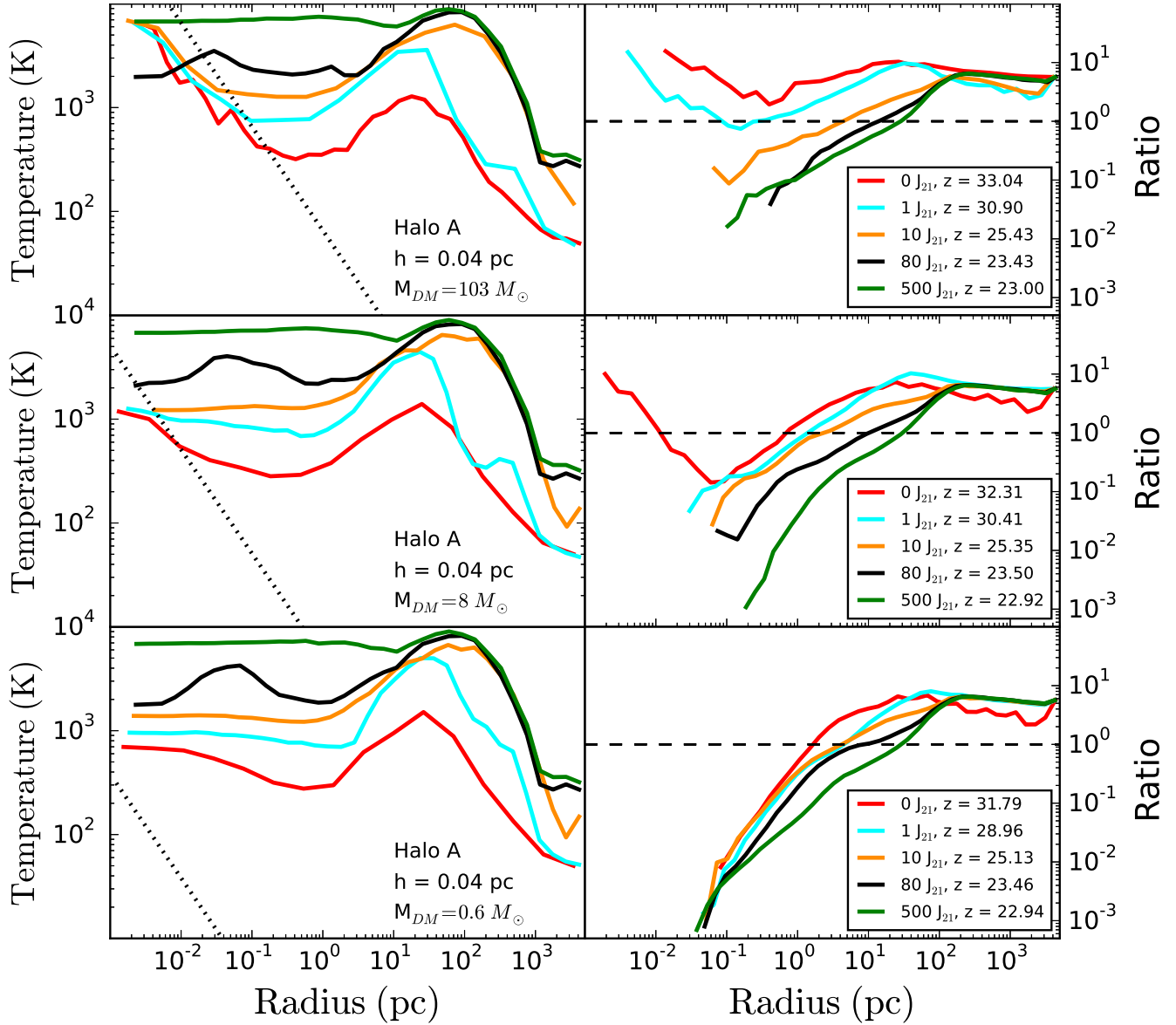


Figure 5. *Halo A*: Each row shows the temperature profile and the ratio of the dark matter enclosed mass to the baryon enclosed mass. The y-axis label is simply identified as “Ratio” for convenience. The top row shows the case where the particle mass is set to $M_{DM} = 103 M_{\odot}$ and no smoothing is employed. The dark matter mass resolution then varies between each row with every other parameter remaining unchanged. In each individual panel the external field varies between $0 J_{21}$ and $500 J_{21}$. The dotted line in the left hand panels is the “discretisation temperature” as defined in equation 4. At a given scale it shows the effect a dark matter particle of a given mass can have on the baryon temperature.

ticular, we choose three further field amplitudes of $0 J_{21}$ (i.e. no background radiation), $1 J_{21}$ and $10 J_{21}$. To test for any discreteness effects from under-resolved dark matter particles we do not smooth the particles onto the grid so the smoothing length is set to the cell size of the finest grid - 0.04 comoving parsecs in each case.

In Figure 5 we have plotted the radial profiles of the temperature and the dark matter mass to gas ratio with the mass resolution increasing between each panel as indicated in the right hand column of the figure.

Examining first the top panel where the dark matter particle resolution is set to $M_{DM} = 103 M_{\odot}$ we see

that the simulations with lower field amplitudes ($0 J_{21}$, $1 J_{21}$ and $10 J_{21}$) all show a strong temperature increase towards the core of the halo. As the mass resolution is increased (middle and bottom rows) this phenomenon disappears and the temperature profiles converge to temperatures close to $T \sim 1000$ K as would be expected for the formation of metal-free stars at this redshift (Abel et al. 2002; Yoshida et al. 2006, 2008; Bromm et al. 2009; Smith et al. 2009; Turk et al. 2009; Stacy et al. 2010; Clark et al. 2011a; Stacy & Bromm 2014).

In the lowest mass resolution simulations this spurious behaviour can be explained by examining the dark matter

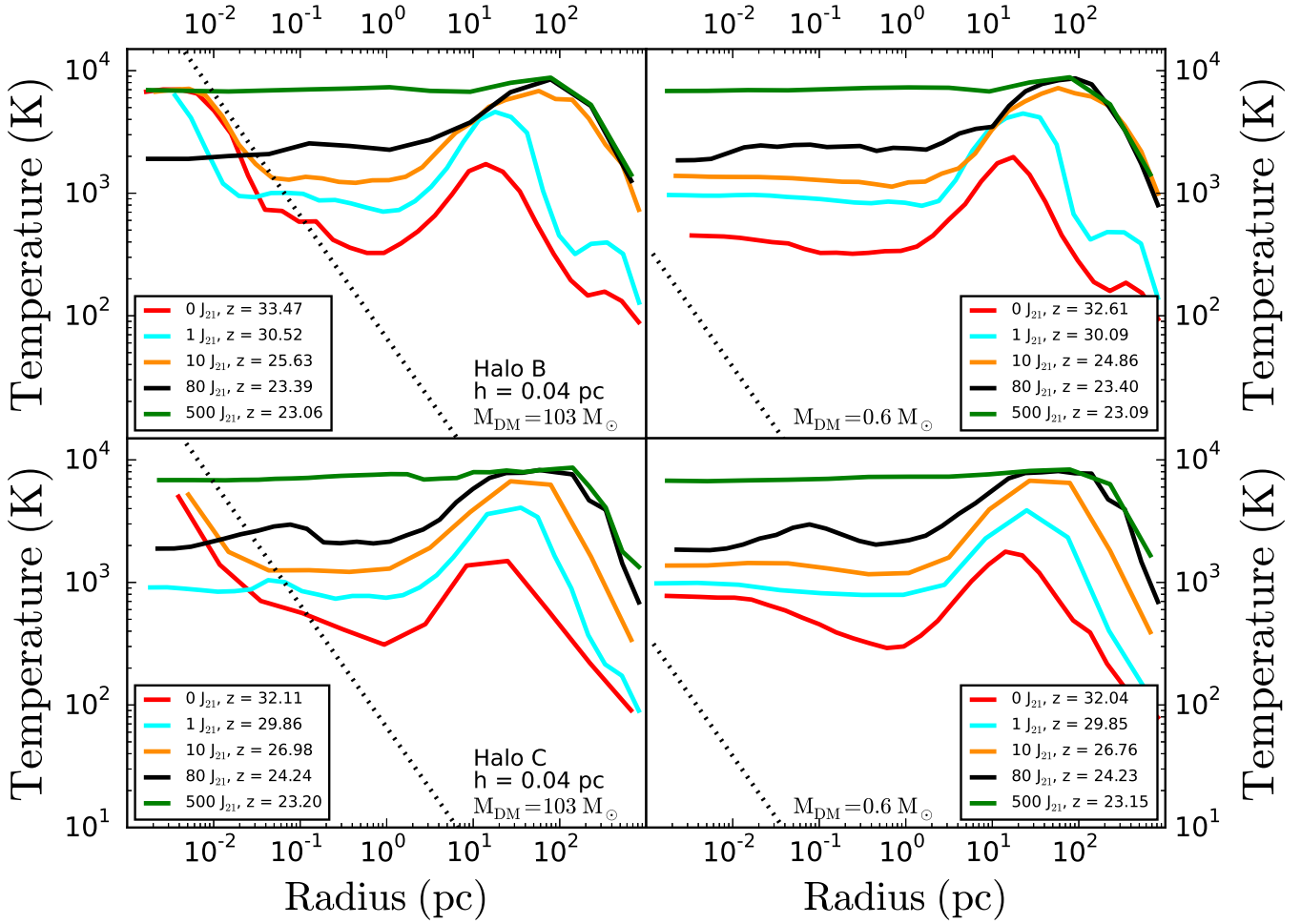


Figure 6. *Halo B & Halo C:* The temperature profile for haloes B & C are shown for two different dark matter particle resolutions. Halo B is shown in the top row while halo C is displayed in the bottom row. The particle resolution is set at $M_{\text{DM}} = 103 M_{\odot}$ in the left hand column while it is set to $M_{\text{DM}} = 0.6 M_{\odot}$ in the right hand column. The dotted line in each panel is our analytical estimate of the discretisation temperature, $T_{\text{disc}}(R)$.

to gas ratio in the right hand column. In the lowest mass resolution simulations ($M_{\text{DM}} = 103 M_{\odot}$, top right panel) the simulations with external radiation amplitudes of 0 J_{21} , 1 J_{21} and 10 J_{21} are all dark matter dominated (or only mildly gas dominated) within the core of the halo resulting in spurious heating of the gas due to the presence of large dark matter particles (we saw this before in Figure 3 for example). As we increase the dark matter particle resolution we see this behaviour disappear as the dark matter to gas ratio drops significantly and the temperature profiles converge to $T \sim 1000$ K as expected.

In the temperature panels (left hand panels) we have also overplotted our analytical estimation of the discretisation temperature, $T_{\text{disc}}(R)$, (see equation 4). This gives the scale at which we expect the dark matter particle mass to start to impact (negatively) on the temperature. In the top left panel we see that the large dark matter particle mass used here ($M_{\text{DM}} = 103 M_{\odot}$) means that the $T_{\text{disc}}(R)$ function intersects the 0 J_{21} profile very close to where the baryon temperature starts to show a spurious increase. A

similar effect is seen in the middle left panel where the particle mass is set to ($M_{\text{DM}} = 8 M_{\odot}$). In the bottom left panel the $T_{\text{disc}}(R)$ function does not intersect any of the temperature profile lines. This indicates that at this particle resolution we would not expect any impact from dark matter heating effects at the spatial scales probed in our simulations and this is exactly what we see.

Taking the field strength of 1 J_{21} as the fiducial case we find that the core (< 1 pc) of the simulation was resolved by only 36 dark matter particles (with a $V_{\text{disc}} \sim 18$ km/s and $T_{\text{disc}} \sim 47000$ K) when the mass resolution was set to $M_{\text{DM}} = 103 M_{\odot}$. When the resolution was increased to $M_{\text{DM}} = 8 M_{\odot}$ the number of dark matter particles in the core increased to 473 particles ($V_{\text{disc}} \sim 5$ km/s and $T_{\text{disc}} \sim 3600$ K) and increasing the resolution to $M_{\text{DM}} = 0.6 M_{\odot}$ resulted in the core being resolved by 3072 particles ($V_{\text{disc}} \sim 1$ km/s and $T_{\text{disc}} \sim 300$ K).

The smaller haloes, those with a gas core less than $\sim 10^4 M_{\odot}$, which collapse when the external field amplitude is relatively small require a much higher dark matter resolution.

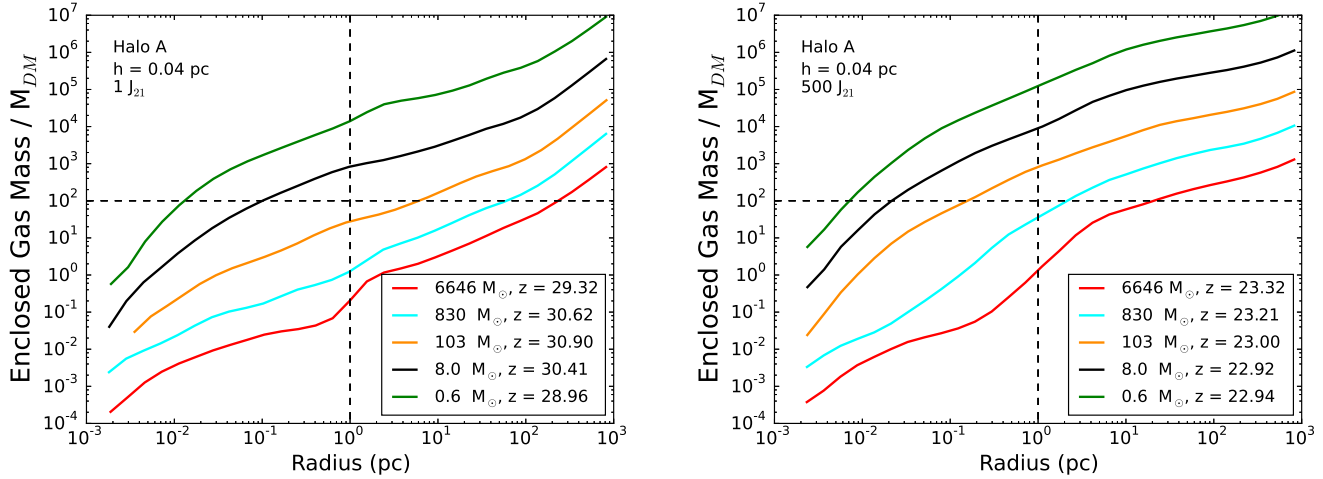


Figure 7. *Halo A*: Radial profiles of the enclosed baryonic mass divided by the mass of the (minimum) dark matter particle mass, M_{DM} , used in each simulation. In order to satisfy our resolution requirement the ratio of the enclosed baryonic mass to the dark matter particle mass should exceed 100.0 at a radius of 1 parsec. In the left hand panel the external radiation field is set to 1 J_{21} while in the right hand panel the radius is set to 500 J_{21} . The dashed lines marks the radius at 1 pc (vertical dashed line) and the ratio value of 100 (horizontal dashed line).

In this case we find that the dark matter particle size must be less than $\sim 8 M_{\odot}$ (although even at $M_{DM} \sim 8 M_{\odot}$ we see some spurious heating of the core for the case of $J = 0$ J_{21}) and ideally less than $\sim 1 M_{\odot}$ in order to ensure that the core of the halo is dominated by baryons and not by spuriously large dark matter particles.

4.4 Comparing Halo B and Halo C

We now briefly examine the hydrodynamic properties of Halo B and Halo C. In Figure 6 we have plotted the temperature profiles of Halo B and Halo C. Halo B and Halo C, similar to Halo A, represent high sigma peaks in the density field. As a result they contain a halo which collapses early even when exposed to a strong external radiation field i.e. the collapse redshift when the external field is set to 500 J_{21} is $z_{col} \sim 23.1$ for Halo B and $z_{col} \sim 23.2$ for Halo C. The top row of Figure 6 contains plots from Halo B and the bottom row is for Halo C. The mass resolution is set at $M_{DM} = 103 M_{\odot}$ in the left hand column and $M_{DM} = 0.6 M_{\odot}$ in the right hand column as indicated. No smoothing of the dark matter particles is employed. The external field is varied in each panel to show the effect that the external radiation field and the dark matter resolution has on the forming halo in each case. Finally, we also overplot $T_{disc}(R)$ (equation 4) as a dotted line in each panel.

Both haloes display very similar properties to Halo A (Figure 5). For low field strengths ($J \lesssim 10 J_{21}$) and $M_{DM} = 103 M_{\odot}$ the temperature increases strongly within the core of the halo resulting in temperatures close to $T \sim 10^4$ K. This spurious heating in the core of the halo is caused by a dark matter particle mass that is too coarse. The large dark matter particle masses induce perturbing forces on the gas which heats the core. This conclusion is supported by our analytical estimate of the heating effect given by $T_{disc}(R)$. In left hand panels, where the mass res-

olution is comparatively poor, the temperature profiles for the low J_{21} values begin to increase in the core at a radius very close to where the analytical estimate predicts that heat may be imparted from dark matter interactions.

However, increasing the mass resolution to $M_{DM} = 0.6 M_{\odot}$ resolves this spurious heating and in this case the temperatures converge to $T \sim 1000$ K as seen for Halo A in Figure 5. Again we see this through out analytical estimate of the temperature as well. In the right hand panels $T_{disc}(R)$ is always below the temperature of the baryons and hence has no effect on the thermal physics at the scales probed in these simulations. Similar to the results for Halo A it is clearly demonstrated that for small external radiation fields and hence core masses $M_{core} \lesssim 10^4 M_{\odot}$, a dark matter particle mass of $M_{DM} \sim 1 M_{\odot}$ is required.

For field strengths with $J \gtrsim \text{few} \times 10 J_{21}$ a very high resolution dark matter particle is not required and in these cases a particle mass of $M_{DM} \sim 100 M_{\odot}$ is adequate due to the more massive gas core in these cases.

5 CHOOSING THE CORRECT DARK MATTER PARTICLE SIZE

Using a suite of simulations we attempted to constrain the dark matter resolution required to achieve convergence in the baryonic properties of haloes collapsing at high redshift. The particle mass required depends only very weakly on the halo (we see no differences between the three haloes simulated) but depends strongly on the enclosed baryonic mass within the core of the halo (here defined as the radius at which the baryonic enclosed mass exceeds the dark matter enclosed mass - typically occurring between 1 parsec and 10 parsecs in our simulations). We used different external radiation fields which has the effect of varying the mass of the core that forms and the cooling processes available in the collapsing halo.

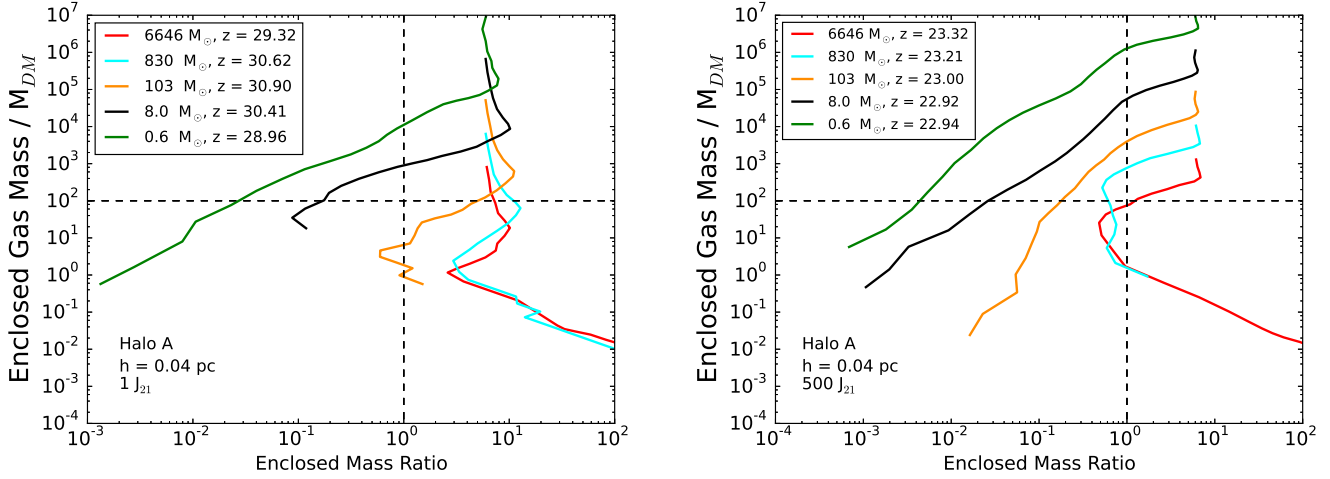


Figure 8. *Halo A*: Radial profiles of the enclosed baryonic mass divided by the mass of the (minimum) dark matter particle mass, M_{DM} , used in each simulation. The scaling ratio is this time plotted against the enclosed mass ratio (i.e. enclosed dark matter mass divided by enclosed baryon mass). The dashed lines marks the point of baryon - dark matter enclosed mass equality (vertical dashed line) and the ratio value of 100 (horizontal dashed line).

In Figure 7 we have plotted the enclosed baryon mass scaled by the minimum dark matter particle mass used in each simulation against the radius. We show the results for two representative cases; $J = 1 J_{21}$ in the left hand panel and $J = 500 J_{21}$ in the right hand panel. From our previous results we know that when the external field is set to $1 J_{21}$ then a dark matter resolution of $M_{\text{DM}} < 103.0 M_{\odot}$ is required. On the other hand when the field strength is set to $500 J_{21}$ then a dark matter resolution of $M_{\text{DM}} < 830.0 M_{\odot}$ is sufficient.

In the case where $J = 1 J_{21}$ we see that the required mass resolutions (S8 and S06) have a ratio of the enclosed mass within the core, M_{core} , to the dark matter particle mass, M_{DM} , of > 100 at the core radius i.e. $M_{\text{core}}/M_{\text{DM}} > 100.0$. Similarly, in the case where $J = 500 J_{21}$ we see that three dark matter particle masses satisfy the criterion that $M_{\text{core}}/M_{\text{DM}} > 100.0$ and we have found previously that these three particle masses ($M_{\text{DM}} = 103 M_{\odot}$, $M_{\text{DM}} = 8 M_{\odot}$ and $M_{\text{DM}} = 0.6 M_{\odot}$) produce converged results for this field strength (or equivalently baryonic core mass since the accretion rate depends on the core temperature which depends on the radiation field strength).

In Figure 8 we have plotted the enclosed baryon mass scaled by the minimum dark matter particle mass against the enclosed mass ratio (i.e. enclosed dark matter mass divided by enclosed baryon mass). The representation clarifies that the scaling ratio must exceed a value of 100.0 at the point of baryon - dark matter enclosed mass equality (and the core must also remain baryon dominated) in order to fulfill our resolution requirements as found previously.

We therefore present this empirically derived result as a “rule of thumb” -

$$M_{\text{core}}/M_{\text{DM}} > 100.0 \quad (5)$$

The minimum dark matter particle mass used must be a factor of one hundred less than the baryonic mass contained within a sphere in which the baryon mass dominates.

However, we caution that this relationship does not provide a sufficient condition. It should instead be used as a starting point for conducting convergence tests for high redshift collapse simulations. Our simulations indicate that failing to adhere to this relationship will most likely produce spurious results and at the very least this relationship should be satisfied and convergence checked before performing full production runs.

6 CONCLUSIONS

We have conducted a comprehensive study of the dark matter particle resolution requirements necessary to study the collapse of gas at high redshift in the presence of a background radiation field below the Lyman limit. We have used the publicly available **Enzo** code to conduct the study. **Enzo**, like most other grid (and particle) based codes, represents dark matter as discrete particles while solving the hydrodynamic equations on a Eulerian grid. In this light, we tested a number of different parameters that can potentially affect the interaction of the dark matter particles with the collapsing baryonic core.

We investigated the effect of “smoothing” the dark matter particles onto the grid in regions of very high density in order to negate any two body scattering effects that may occur when the cell size becomes very small. We probed the effect of increasing the dark matter resolution around regions of interest by employing a particle splitting algorithm and tested its effectiveness. Furthermore, we varied the background radiation field from having no external radiation, $J = 0 J_{21}$, up to $J = 500 J_{21}$ where J_{21} is in the usual units of $1 \times 10^{-21} \text{ erg cm}^{-2} \text{ s}^{-1} \text{ Hz}^{-1} \text{ sr}^{-1}$.

We find that smoothing particles onto the grid provides some relief from the effects of spurious two body dark matter interactions and is most effective when the dark matter resolution is already comparatively high. With a dark matter particle mass of $M_{\text{DM}} \lesssim 100 M_{\odot}$, smoothing the particles

onto the grid produces more converged results, when compared against the non-smoothed case, as the dark matter resolution is increased but nonetheless having a high dark matter resolution was the crucial and overriding factor. At more intermediate particle masses, $M_{\text{DM}} \gtrsim 100 M_{\odot}$, smoothing can alleviate some of the effects of two-body scattering (compared to the unsmoothed case) but it cannot negate them entirely and is somewhat case (halo) dependent. When the dark matter mass resolution is low (i.e. $M_{\text{DM}} \gtrsim 1000 M_{\odot}$) smoothing provided no extra positive effect to alleviate spurious effects as expected.

In summary, smoothing is most effective when the dark matter resolution is already high as it wipes out any lingering discreteness effects. It is significantly less effective as the mass resolution drops and it should not be seen as a fix for under resolved dark matter simulations. As a result we advocate the use of smoothing *in conjunction with* high particle resolution only.

In examining the effectiveness of particle splitting we find very encouraging results. We initially tested the effect of splitting on the properties of dark matter in dark matter only simulations and found that the splitting added little or no additional numerical noise to the results finding that dark matter density profiles and enclosed mass profiles remained highly converged both before and after splitting. After adding in baryons, splitting the dark matter enabled us to remove spurious dark matter effects from otherwise under-resolved simulations.

Using an external radiation field with an energy below the Lyman limit we found that the particle mass required varied with the strength of the radiation field. This is not surprising since a strong radiation field effectively dissociated H_2 (and its pathway element H^-) reducing the cooling ability of the halo thus increasing the accretion rate making it more massive. We found that as the halo grew the dark matter particle mass required also grew (i.e. less dark matter resolution was required). This means that when one is examining the affect that a very strong radiation field has on a collapsing halo the dark matter particle mass may be greater (by several factors), without any loss in numerical accuracy, compared to case where haloes are collapsing in the absence of an external radiation field or in the presence of a weak background field.

We find that a useful “rule of thumb” is that the ratio of the enclosed baryonic mass within the core of the halo to the individual dark matter mass must exceed 100 i.e. $M_{\text{core}}/M_{\text{DM}} > 100.0$. We found that, for the simulations conducted here, this relationship must always be satisfied to produce converged results. We therefore advise that this relationship always be fulfilled and that appropriate convergence tests be conducted in parallel to ensure reliable results.

While this study was carried out using the grid code **Enzo** we expect the results to hold for other grid and non-grid codes (e.g. SPH codes) that use the N-body technique to represent the dark matter component. On a final note it is appropriate to mention the recent work of Hahn & Angulo (2015) who describe a method to follow the dark matter evolution using a six dimensional phase approach rather than the traditional N-body model studied here. Their approach dispenses with the discrete nature of the N-body method and may help to significantly suppress any discreteness ef-

fects that can arise in modelling collisionless systems in the future.

ACKNOWLEDGEMENTS

J.A.R. and P.H.J. acknowledge the support of the Magnus Ehrnrooth Foundation, the Research Funds of the University of Helsinki and the Academy of Finland grant 274931. J.H.W. acknowledges support by NSF grants AST-1211626 and AST-1333360. The numerical simulations were performed on facilities hosted by the CSC -IT Center for Science in Espoo, Finland, which are financed by the Finnish ministry of education. Computations described in this work were performed using the publicly-available **Enzo** code (<http://enzo-project.org>), which is the product of a collaborative effort of many independent scientists from numerous institutions around the world. Their commitment to open science has helped make this work possible. The freely available astrophysical analysis code YT (Turk et al. 2011b) was used to construct numerous plots within this paper. The authors would like to express their gratitude to Matt Turk et al. for an excellent software package. J.A.R. would also like to thank Greg Bryan for useful discussions leading to this work. Finally, we would like to thank the referee, Greg Bryan, for a very detailed report which greatly enhanced the final manuscript.

REFERENCES

- Aarseth S. J., 1963, MNRAS, 126, 223
- Abel T., Anninos P., Zhang Y., Norman M. L., 1997, New Astronomy, 2, 181
- Abel T., Bryan G. L., Norman M. L., 2002, Science, 295, 93
- Agarwal B., Dalla Vecchia C., Johnson J. L., Khochfar S., Paardekooper J. P., 2014, MNRAS, 443, 648
- Barnes J., Hut P., 1986, Nature, 324, 446
- Barnes J. E., Hut P., 1989, ApJS, 70, 389
- Begelman M. C., Volonteri M., Rees M. J., 2006, MNRAS, 370, 289
- Bertschinger E., 1998, ARA&A, 36, 599
- Bosch F. C. v. d., Jiang F., Hearin A., Campbell D., Watson D., Padmanabhan N., 2014, MNRAS, 445, 1713
- Bovino S., Schleicher D. R. G., Grassi T., 2014, A&A, 561, A13
- Bromm V., Larson R. B., 2004, ARA&A, 42, 79
- Bromm V., Loeb A., 2003, ApJ, 596, 34
- Bromm V., Coppi P. S., Larson R. B., 1999, ApJ, 527, L5
- Bromm V., Coppi P. S., Larson R. B., 2002, ApJ, 564, 23
- Bromm V., Yoshida N., Hernquist L., McKee C. F., 2009, Nature, 459, 49
- Bryan G. L., Norman M. L., 1995, Bulletin of the American Astronomical Society, 27, 1421
- Bryan G. L., Norman M. L., 1997, in ASP Conf. Ser. 123: Computational Astrophysics; 12th Kingston Meeting on Theoretical Astrophysics. pp. 363–+
- Bryan G. L., Norman M. L., Stone J. M., Cen R., Ostriker J. P., 1995, Computer Physics Communications, 89, 149

- Bryan G. L., Norman M. L., O'Shea B. W., Abel T., Wise J. H., Turk M. J., The Enzo Collaboration, 2014, *ApJS*, 211, 19
- Cen R., Miralda-Escudé J., Ostriker J. P., Rauch M., 1994, *ApJ*, 437, L9
- Cen R. Y., Ostriker J. P., Jameson A., Liu F., 1990, *ApJ*, 362, L41
- Clark P. C., Glover S. C. O., Klessen R. S., Bromm V., 2011a, *ApJ*, 727, 110
- Clark P. C., Glover S. C. O., Smith R. J., Greif T. H., Klessen R. S., Bromm V., 2011b, *Science*, 331, 1040
- Couchman H. M. P., 1991, *ApJ*, 368, L23
- Croton D. J. et al., 2006, *MNRAS*, 365, 11
- Davis M., Efstathiou G., Frenk C. S., White S. D. M., 1985, *ApJ*, 292, 371
- Diemand J., Kuhlen M., Madau P., Zemp M., Moore B., Potter D., Stadel J., 2008, *Nature*, 454, 735
- Dijkstra M., Haiman Z., Mesinger A., Wyithe J. S. B., 2008, *MNRAS*, 391, 1961
- Efstathiou G., Davis M., White S. D. M., Frenk C. S., 1985, *ApJS*, 57, 241
- Forrey R. C., 2013, *ApJ*, 773, L25
- Frenk C. S., White S. D. M., Davis M., Efstathiou G., 1988, *ApJ*, 327, 507
- Gelb J. M., Bertschinger E., 1994, *ApJ*, 436, 467
- Gingold R. A., Monaghan J. J., 1977, *MNRAS*, 181, 375
- Greif T. H., Springel V., White S. D. M., Glover S. C. O., Clark P. C., Smith R. J., Klessen R. S., Bromm V., 2011, *ApJ*, 737, 75
- Hahn O., Abel T., 2011, *MNRAS*, 415, 2101
- Hahn O., Angulo R. E., 2015, *ArXiv e-prints*:1501.01959
- Haiman Z., 2006, *New Astronomy Review*, 50, 672
- Haiman Z., Loeb A., 2001, *ApJ*, 552, 459
- Hernquist L., Katz N., Weinberg D. H., Miralda-Escudé J., 1996, *ApJ*, 457, L51
- Hirano S., Hosokawa T., Yoshida N., Umeda H., Omukai K., Chiaki G., Yorke H. W., 2014, *ApJ*, 781, 60
- Hockney R. W., Eastwood J. W., 1988, *Computer simulation using particles*. Bristol: Hilger, 1988
- Hozumi S., 1997, *ApJ*, 487, 617
- Jenkins A., Frenk C. S., White S. D. M., Colberg J. M., Cole S., Evrard A. E., Couchman H. M. P., Yoshida N., 2001, *MNRAS*, 321, 372
- Johansson P. H., Naab T., Ostriker J. P., 2012, *ApJ*, 754, 115
- Johnson J. L., Whalen D. J., Li H., Holz D. E., 2013, *ApJ*, 771, 116
- Kaufmann T., Mayer L., Wadsley J., Stadel J., Moore B., 2006, *MNRAS*, 370, 1612
- Kim J. h., Wise J. H., Alvarez M. A., Abel T., 2011, *ApJ*, 738, 54
- Kitsionas S., Whitworth A. P., 2002, *MNRAS*, 330, 129
- Latif M. A., Schleicher D. R. G., Schmidt W., Niemeyer J., 2013, *MNRAS*, 433, 1607
- Latif M. A., Bovino S., Van Borm C., Grassi T., Schleicher D. R. G., Spaans M., 2014a, *MNRAS*, 443, 1979
- Latif M. A., Schleicher D. R. G., Bovino S., Grassi T., Spaans M., 2014b, *ApJ*, 792, 78
- Lucy L. B., 1977, *AJ*, 82, 1013
- Machacek M. E., Bryan G. L., Abel T., 2001, *ApJ*, 548, 509
- Martin P. G., Schwarz D. H., Mandy M. E., 1996, *ApJ*, 461, 265
- Mayer L., Fiacconi D., Bonoli S., Quinn T., Roskar R., Shen S., Wadsley J., 2014, *ArXiv e-prints*:1411.5683
- Navarro J. F., Frenk C. S., White S. D. M., 1996, *ApJ*, 462, 563
- Navarro J. F., Frenk C. S., White S. D. M., 1997, *ApJ*, 490, 493
- Norman M. L., Bryan G. L., 1999, in S.M. Miyama, K. Tomisaka, T. Hanawa, eds, *ASSL Vol. 240: Numerical Astrophysics*. pp. 19–+
- Oh S. P., Haiman Z., 2002, *ApJ*, 569, 558
- O'Shea B. W., Norman M. L., 2008, *ApJ*, 673, 14
- O'Shea B. W., Bryan G., Bordner J., Norman M. L., Abel T., Harkness R., Kritsuk A., 2004, *ArXiv Astrophysics e-prints*:0403.044
- Planck Collaboration et al., 2014, *A&A*, 571, A16
- Rasio F. A., Shapiro S. L., Teukolsky S. A., 1989, *ApJ*, 344, 146
- Regan J. A., Haehnelt M. G., 2009a, *MNRAS*, 396, 343
- Regan J. A., Haehnelt M. G., 2009b, *MNRAS*, 393, 858
- Regan J. A., Johansson P. H., Haehnelt M. G., 2014a, *MNRAS*, 439, 1160
- Regan J. A., Johansson P. H., Wise J. H., 2014b, *ApJ*, 795, 137
- Ryu D., Vishniac E. T., Chiang W. H., 1990, *ApJ*, 354, 389
- Shang C., Bryan G. L., Haiman Z., 2010, *MNRAS*, 402, 1249
- Shlosman I., Hoffman Y., Shaviv G., 1979, *MNRAS*, 189, 723
- Shlosman I., Frank J., Begelman M. C., 1989, *Nature*, 338, 45
- Smith B. D., Turk M. J., Sigurdsson S., O'Shea B. W., Norman M. L., 2009, *ApJ*, 691, 441
- Springel V., 2010, *MNRAS*, 401, 791
- Springel V. et al., 2005, *Nature*, 435, 629
- Springel V. et al., 2008, *MNRAS*, 391, 1685
- Stacy A., Bromm V., 2014, *ApJ*, 785, 73
- Stacy A., Greif T. H., Bromm V., 2010, *MNRAS*, 403, 45
- Stacy A., Greif T. H., Bromm V., 2012, *MNRAS*, 422, 290
- Steinmetz M., 1996, *MNRAS*, 278, 1005
- Steinmetz M., White S. D. M., 1997, *MNRAS*, 288, 545
- Stone J. M., Norman M. L., 1992, *ApJS*, 80, 753
- Susa H., Hasegawa K., Tominaga N., 2014, *ApJ*, 792, 32
- Turk M. J., Abel T., O'Shea B., 2009, *Science*, 325, 601
- Turk M. J., Clark P., Glover S. C. O., Greif T. H., Abel T., Klessen R., Bromm V., 2011a, *ApJ*, 726, 55
- Turk M. J., Smith B. D., Oishi J. S., Skory S., Skillman S. W., Abel T., Norman M. L., 2011b, *ApJS*, 192, 9
- Visbal E., Haiman Z., Bryan G. L., 2014, *MNRAS*, 445, 1056
- Vogelsberger M. et al., 2014, *MNRAS*, 444, 1518
- von Hoerner S., 1960, *Zeitschrift fur Astrophysik*, 50, 184
- von Hoerner S., 1963, *Zeitschrift fur Astrophysik*, 57, 47
- Wambsganss J., Bode P., Ostriker J. P., 2004, *ApJ*, 606, L93
- Warren M. S., Quinn P. J., Salmon J. K., Zurek W. H., 1992, *ApJ*, 399, 405
- White S. D. M., Frenk C. S., 1991, *ApJ*, 379, 52
- White S. D. M., Rees M. J., 1978, *MNRAS*, 183, 341
- Wise J. H., Abel T., 2008, *ApJ*, 685, 40
- Wise J. H., Turk M. J., Abel T., 2008, *ApJ*, 682, 745

- Yoshida N., Abel T., Hernquist L., Sugiyama N., 2003, ApJ, 592, 645
 Yoshida N., Omukai K., Hernquist L., Abel T., 2006, ApJ, 652, 6
 Yoshida N., Omukai K., Hernquist L., 2008, Science, 321, 669

A RUNNING AT THE MAXIMUM REFINEMENT LEVEL

As discussed in §4.1, Figure 9 shows the temperature profile for Halo A for both a non-smoothed (i.e. $h = 0.04$ pc, left panel) and a smoothed run (i.e. $h = 2.8$ pc, right panel) further into its evolution than presented in Figure 3. The simulations are run at the maximum refinement level to examine the further evolution of the core. As mentioned previously, running at the maximum refinement level artificially prevents collapse while the Jeans length is also not resolved. This may potentially induce unphysical results, however we are careful, as detailed below, to only run the simulation for a few timesteps. In this case we plot only the results for the runs in which the collapsing core is gas dominated and therefore exclude simulations S6646 and S830 from both plots so as to exclude any potential dark matter contamination effects which may affect the physical results.

The simulations have been restarted from the last output and allowed to run at the maximum refinement level for a short time ($\sim 130,000$ years). No artificial pressure floor is employed here so as to exclude any artificial heating effects although in principle running at the maximum refinement level without any artificial pressure support can lead to numerical instabilities (Machacek et al. 2001). We are therefore careful to run the simulations only for a few timesteps at this point. As can clearly be seen, as the simulation is allowed to progress, the temperature in the core increases and the core heats up to close to $T \sim 6000$ K in all cases. The reason for this heating is that dense clumps of neutral hydrogen form in the core promoting (collisional) dissociation of H_2 through the reaction



We have used the formulation given in Martin et al. (1996) to model this reaction. The dissociation rate then exceeds the H_2 formation rate in regions within the core of the halo but conversely the formation rate exceeds the dissociating rate in other neighbouring parts resulting in the formation of hot and cold spots within the core of the halo. The formation rate is controlled, at these densities, by the reaction



In Figure 10 we have plotted four projection plots illustrating this effect. The projections are made approximately 130,000 years after reaching the maximum refinement level using a S103 (with no-smoothing) output for illustration (although S8 or S06 could also have been used). In the bottom left panel we show the neutral hydrogen number density showing the formation of a dense core, in the top left panel we show the temperature projection clearly displaying regions of hot and cold gas within the core. The H_2 fraction is shown in the top right panel, reflecting the temperature projection, we see regions of low H_2 fraction surrounded by

regions of high H_2 fraction which dramatically affects the cooling in these regions and causes bumps in the temperature profile as shown in Figure 9. Finally, in the bottom right panel we show the ratio of the H_2 formation rate to the H_2 dissociation rate. Again, we see regions of formation and dissociation within the core consistent with the other projections. The core of the halo is essentially sitting on a knife edge between H_2 formation and dissociation.

It should also be noted that our simulations neglect the potentially important effects of self-shielding. However, a study of the complete effects of self-shielding on the core hydrodynamics is beyond the scope of this paper.

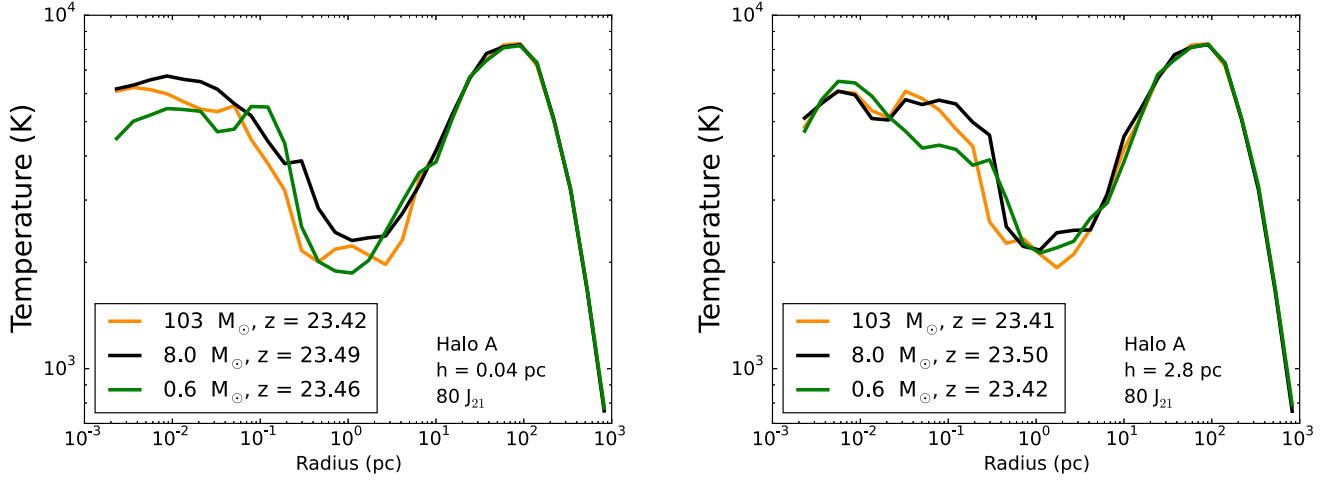


Figure 9. *Halo A*: The left hand panel shows the spherically averaged temperature profile in the centre of the collapsing halo a short time ($\sim 130,000$ years) after running at the maximum refinement level. No smoothing of the dark matter particles occurs in the left hand panel. The right hand panel shows the same temperature profile for simulations in which smoothing of the dark matter particles occurs at 2.8 comoving pc (refinement level 12).

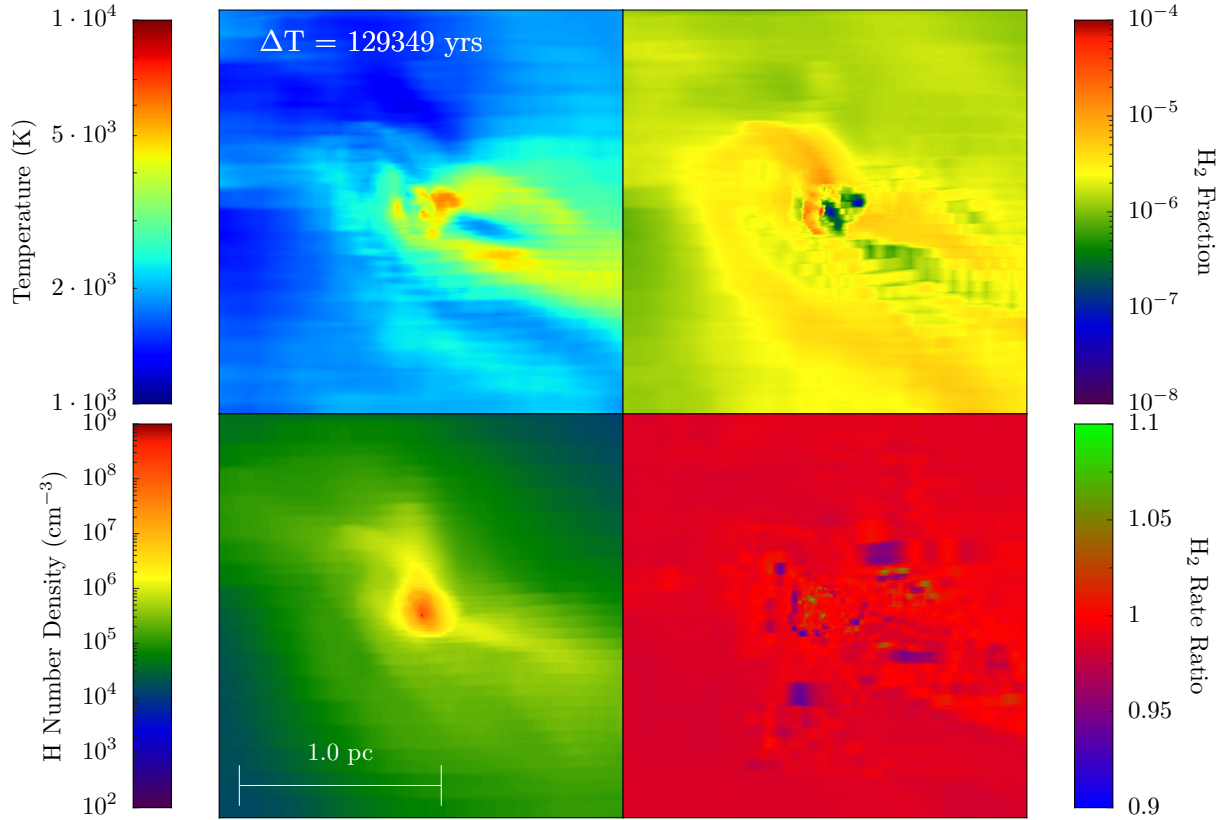


Figure 10. *Halo A*: The four panel projection shows the state of the gas within the core of the halo approximately 130,000 years after reaching the maximum refinement level. Each projection is aligned perpendicular to the angular momentum vector. In the top left panel is shown the temperature projection showing the central “hot” core surrounded by cooler gas. The H_2 fraction is shown in the top right panel and shows that the core contains clumps of molecular gas surrounded by gas where the H_2 fraction is significantly lower. The lower right panel shows the ratio of the H_2 formation rate to the H_2 dissociation rate. Green areas represent areas where H_2 is forming while blue areas represent areas where the H_2 is being dissociated. Finally, in the lower left panel the H number density is shown, in the core of the halo the H number density is at its maximum.